Journal of ELECTRONIC MATERIALS, Vol. 42, No. 3, 2013
DOI: 10.1007/s11664-012-2366-1

Thermal Cycling, Mechanical Degradation, and the Effective Figure of Merit of a Thermoelectric Module

M. T. BARAKO,[1,2] W. PARK,[1] A. M. MARCONNET,[1] M. ASHEGHI,[1] and K. E. GOODSON[1]

1.—Department of Mechanical Engineering, Stanford University, Stanford, CA, USA. 2.—e-mail: mbarako@stanford.edu

Thermoelectric modules experience performance reduction and mechanical failure due to thermomechanical stresses induced by thermal cycling. The present study subjects a thermoelectric module to thermal cycling and evaluates the evolution of its thermoelectric performance through measurements of the thermoelectric figure of merit, ZT, and its individual components. The Seebeck coefficient and thermal conductivity are measured using steady-state infrared microscopy, and the electrical conductivity and ZT are evaluated using the Harman technique. These properties are tracked over many cycles until device failure after 45,000 thermal cycles. The mechanical failure of the TE module is analyzed using high-resolution infrared microscopy and scanning electron microscopy. A reduction in electrical conductivity is the primary mechanism of performance reduction and is likely associated with defects observed during cycling. The effective figure of merit is reduced by 20% through 40,000 cycles and drops by 97% at 45,000 cycles. These results quantify the effect of thermal cycling on a commercial TE module and provide insight into the packaging of a complete TE module for reliable operation.

Key words: Thermoelectric module, infrared microscopy, thermal cycling, figure of merit, Harman method

Nomenclature

A	Cross-sectional area, m^2
I	Electrical current, A
k	Thermal conductivity, $W\ m^{-1}\ K^{-1}$
L	Length of TE element, mm
q	Heat flow, W
q''	Heat flux, $W\ m^{-2}$
T	Temperature, °C
V	Voltage, V
x	Position along direction of conductive heat flow, mm
ZT	Thermoelectric figure of merit

Greek symbols

α	Seebeck coefficient, $V\ K^{-1}$
ρ	Electrical resistivity, Ω m
σ	Electrical conductivity, $\Omega^{-1}\ m^{-1}$

Subscripts

0	At 0 cycles
E	Electrical component of voltage
OC	Open-circuit voltage
pp	Peak-to-peak voltage
ref	Reference layer
TE	Thermoelectric
TE leg	Single thermoelectric leg element
T	Thermoelectrical component of voltage
Total	Total voltage

(Received July 17, 2012; accepted November 16, 2012; published online December 8, 2012)

INTRODUCTION

Thermoelectric (TE) modules provide solid-state conversion between a temperature gradient and an electrical potential. Thermoelectric modules frequently operate in the power generation configuration, where an imposed temperature difference generates an electrical potential and current.

Thermoelectric power generation has been proposed as an efficient method for recovering waste heat, such as in automobile exhaust streams[1–4] and water heaters,[5] and in conjunction with organic Rankine bottoming cycles.[6] Alternatively, when supplied with electrical power, TE modules operate as solid-state heat pumps. This has enabled the miniaturization of some refrigeration systems, such as those used in electronics cooling[7] and scalable climate control.[8] Thermoelectric modules are silent, scalable, and contain no moving parts, but efficiency limitations have historically restricted these devices to niche applications where conventional refrigeration or power generation cycles are not practical, such as radioisotope power generation in deep-space satellites[2] and onboard power generation for implanted medical devices.[9] Recent scientific efforts have focused on improving the efficiency through thermoelectric material improvements using nanostructures to tune the thermal conductivity, electrical conductivity, and Seebeck coefficient.[10,11]

A typical TE module consists of many semiconductor legs connected electrically in series and thermally in parallel. The legs alternate between *n*- and *p*-type thermoelectric materials (typically Bi_2Te_3 alloys for commercial modules). Often these legs are soldered to copper interconnects, which creates a thermally conductive but mechanically brittle metallic bond. The inherently large number of thermal cycles and thermal shocks during typical operation lead to performance reduction and device failure.[12] The mismatch of thermal expansion coefficients between the bonded materials leads to thermomechanical stresses at the leg–interconnect solder interfaces. Thermal cycling is characteristic of many thermoelectric applications and results in mechanical degradation of the interfaces.[13,14] Thermal cycling of TE modules is common for both refrigeration and electricity generation applications. Repeated thermal cycling leads to stresses and defects at the brittle solder interfaces and can also induce material diffusion in the semiconductor legs and copper interconnects. The present work seeks to understand and quantify the effects of thermal cycling on the performance of a commercial TE module by observing the evolution of the thermoelectric properties and figure of merit during thermal cycling until device failure.

The standard TE performance metric is the nondimensional figure of merit, ZT, which depends on the thermal conductivity k, the electrical conductivity σ, and the Seebeck coefficient α.

$$ZT = \frac{\sigma\alpha^2}{k}T, \tag{1}$$

where T is the average temperature of the module (taken as the average of the hot- and cold-side temperatures). In this work, we measure both the individual components of ZT and the value of ZT directly, as well as the evolution of these parameters with thermal cycling. The effects of thermal cycling are examined by imposing a square-wave voltage across the TE module to generate a temperature difference across the module. During thermal cycling, one side of the module is exposed to ambient convection and heats to +146°C and cools to −20°C over each 60 s period of the square-wave voltage. The other side of the module is maintained at isothermal conditions (23°C) using a copper heat exchanger. The module properties are measured at periodic cycling intervals, where the thermal conductivity and Seebeck coefficient of the TE module are measured using a steady-state cross-sectional infrared thermometry technique. The electrical conductivity is determined using a direct-current (DC) electrical technique, and ZT is directly measured using the Harman technique.[15]

EXPERIMENTAL PROCEDURES

Thermal Cycling

Thermal cycling is used to simulate the actual operation that is characteristic of many thermoelectric applications and to reproduce this environment under laboratory conditions and timescales. The TE module is clamped to a copper heat sink with a thin layer of thermal grease (Omegatherm 201) at the interface. This maintains one side of the TE module at approximately 23°C during cycling, while the other side is exposed to ambient natural convection. A DC voltage source applies a square-wave voltage across the TE module, oscillating between +2.3 V and −2.3 V with a period of 60 s, to induce a temperature gradient across the module as shown in Fig. 1. This voltage is chosen as it is the maximum rated voltage for this particular commercial module. This signal causes the convective side of the TE module to oscillate between +146°C and −20°C, corresponding to 95% of the steady-state temperatures for +2.3 V and −2.3 V, respectively. The large thermal mass of the heat sink maintains the other surface temperature of the TE module at ∼23°C over the duration of a complete thermal cycle. At predetermined intervals, the thermal cycling is stopped and the thermoelectric properties of the TE module are measured. The structure is clamped together to apply uniform compressive pressure (∼3 MPa while isothermal at room temperature), analogous to the mechanical boundary conditions under operating conditions in typical thermoelectric applications. This constrains the periodic thermal expansion, which facilitates the formation of thermomechanical stresses in the module and at the interfaces.

In this work, the module is tested in a Peltier cooling configuration, i.e., the applied voltage induces a temperature difference, rather than a power generation configuration. The supplied voltage serves to establish a temperature gradient and to impose stresses on the module. These thermomechanical stresses appear to be the dominant

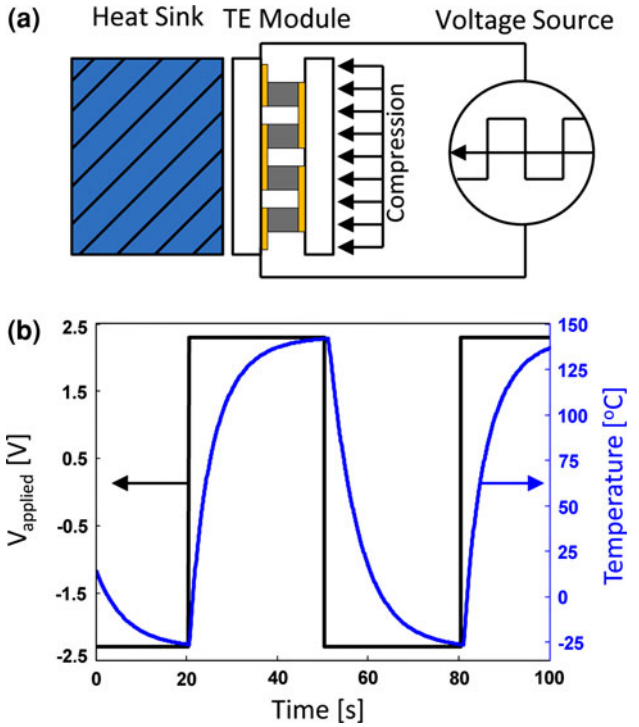

Fig. 1. (a) The TE module is placed with one side against a copper heat sink which is isothermal at 23°C. The module is clamped to the heat sink. This provides moderate compressive pressure to more closely represent the mechanical boundary conditions of a thermoelectric application. (b) A square-wave voltage (black) is applied with $V_{pp} = \pm 2.3$ V and a period of 60 s. This voltage induces a temperature profile where the open air side of the TE module (blue) oscillates between 146°C and −20°C while the isothermal side remains near 23°C.

failure mode, and therefore this cycling configuration is representative of systems in both Peltier cooling and power generation applications. It has been suggested that both compositional and structural changes contribute to device failure.[16] Electromigration of molecular species due to charge transport, thermal gradients, and the presence of an electric field in the TE materials, the solders, and the interconnects also leads to device degradation and failure.[17] While this has been shown to contribute to TE performance reduction, this specific effect is not independently examined in the present work.

Infrared Microscopy of the Effective Thermal Conductivity and Seebeck Coefficient

Infrared (IR) microscopy is a noninvasive temperature measurement technique that generates a high-resolution two-dimensional temperature map of a surface. This temperature map is used to determine the thermal conductivity and Seebeck coefficient of the TE module. The IR microscope (Quantum Focus Instruments) provides a maximum spatial resolution up to the diffraction limit of 3 μm to 5 μm. For calibration, the TE module is first heated externally from both sides to uniformly raise the temperature of the module to 70°C, which is measured by thermocouples embedded in the copper attachments on each side. The cross-sectional surface of the TE module is then spray-coated with a thin layer of graphite (LU204; Sprayon Products) to increase the emissivity to nearly unity and to improve the uniformity of the radiant emission from the surface. A radiance map is recorded and used to compare the radiance of each pixel with that of a blackbody at the same temperature. This yields an emissivity map which corrects for nonideal emissive properties of the surface and accounts for variations in surface conditions. As the temperature changes, the emissivity and measured radiance of the surface are used to determine the temperature at each point in the field of view, generating a temperature map. The emissivity (recorded at 70°C, which is approximately the mean temperature of the measurement) is assumed to be independent of temperature. This is verified continuously during the measurement by comparing the temperatures at the boundaries of the IR temperature map (the heat source and heat sink) with values measured by thermocouples at the same location. At all times these independent temperature measurements remain consistent to within 1°C, and any temperature dependence of emissivity is not significant compared with other sources of uncertainty.

The thermal conductivity is determined from this IR temperature map by using a comparative technique where reference layers are placed in thermal series with the TE module. Fused silica is chosen as the reference layer since it has a thermal conductivity ($k_{ref} = 1.4$ W m^{-1} K^{-1}) comparable to thermoelectric elements. These reference layers are placed on both sides of the TE module and are used to determine the heat flux conducting through this three-layer stack. One side of this stack is then heated via an external electrical heater and the other side is maintained at ~10°C using a chilled water heat exchanger. Once steady-state conditions are reached, a two-dimensional temperature map is recorded, as shown in Fig. 2. The temperature gradient in each layer i is governed by Fourier's Law

$$q = q_i'' A_i = k_i A_i \frac{\mathrm{dT_i}}{\mathrm{d}x}, \tag{2}$$

where q_i'' is the heat flux in the x-direction, A_i is the cross-sectional area, k_i is the thermal conductivity, and $\mathrm{d}T_i/\mathrm{d}x$ is the temperature gradient within the ith layer. Since all of the layers are thermally in series, the same quantity of heat conducts through the reference layers and the TE module if convective and radiative effects are negligible. This assumption is validated through the use of two reference layers, which permit the quantification of heat losses by convection and radiation. The difference between the heat conducted through the hot-side

reference layer and the cold-side reference layer corresponds to the heat dissipated over the length of the stack. For all measurements this difference is found to be less than 10% of the total heat flux, and it is therefore assumed that conduction is the primary mode of heat transfer for the analysis. These two heat flux values also serve as an upper and lower bound for estimating the actual heat flux conducted through the TE module. The temperature map is recorded, containing both reference layers and the cross-section of the TE module. Since heat flow is one dimensional, the two-dimensional temperature map is averaged in the direction perpendicular to the heat flux to reduce the effects of experimental noise. This yields a one-dimensional temperature profile along the length of the conductive heat flux vector (Fig. 3). Using Fourier's Law, the thermal conductivity of each TE leg is calculated by comparing the heat conducted through the reference layers with the temperature gradient and area of the TE leg.

$$\frac{k_{\mathrm{TE}}}{k_{\mathrm{ref}}} = \frac{A_{\mathrm{ref}}\left(\frac{\mathrm{dT}}{\mathrm{dx}}\right)_{\mathrm{ref}}}{A_{\mathrm{TE}}\left(\frac{\mathrm{dT}}{\mathrm{dx}}\right)_{\mathrm{TE}}}. \tag{3}$$

The average thermal conductivity of the two legs is computed using Eq. 3 for a single pair of n- and p-type legs, where A_{TE} is the combined cross-sectional area of the two legs. This implicitly assumes that each TE leg conducts the same heat flux, which is validated by measuring the temperature gradient in each leg to differ by approximately 2.5%. A temperature map is measured for a range of different hot-side temperatures from 50°C to 130°C while maintaining a cold-side temperature of ~10°C. For each heat flux conducted through the sample, the temperature gradient in the two adjacent TE legs is measured and averaged. The same two TE legs are measured at each cycling interval to ensure consistency.

The Seebeck coefficient is calculated by simultaneously measuring the open-circuit DC voltage while recording the IR temperature map. The temperature difference is measured across the TE elements inside the module, which enables the temperature to be recorded at the exact location where the voltage is measured. This allows for a more accurate and less invasive temperature measurement compared with external thermocouples. In contrast, thermocouples require physical contact to the modules and can be difficult to precisely locate on the TE module. Thermocouples also provide a parallel conduction pathway and introduce a thermal contact resistance which can affect the accuracy of the measured temperature and voltage. IR imaging directly probes the temperature field inside of the module without

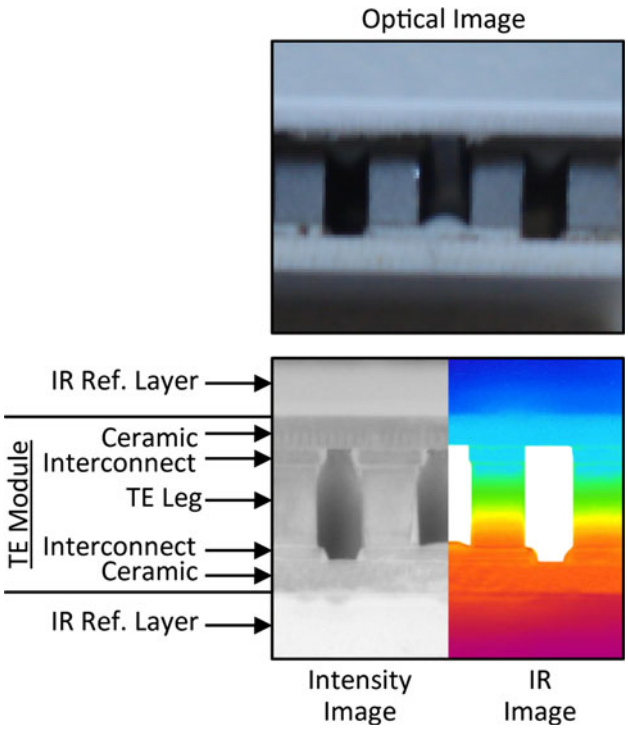

Fig. 2. (Top) Optical microscopy image of a TE module, highlighting the ceramic supports, copper interconnects, and semiconductor legs. (Bottom) Infrared image of the cross-section of a TE module. The grayscale intensity image (left) shows the radiation intensity, while the false-color image (right) indicates the spatially varying temperature profile.

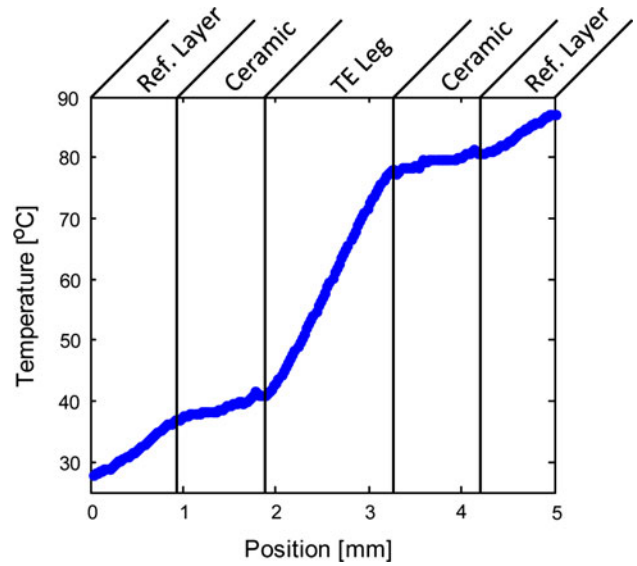

Fig. 3. Cross-sectional temperature profile of a TE module. Fused silica reference layers are placed on both sides of the TE module as reference layers for thermal measurements. As heat conducts through the structure, a temperature profile is set up and the relative magnitude of the linear temperature gradients and sudden temperature drops relate to the thermal conductivity and thermal boundary resistances, respectively. The slope of each region is determined using a linear least-squares fit. The temperature drop across the TE elements inside the module is used to determine both the thermal conductivity and the Seebeck coefficient of the module. The layers labeled "ceramic" also include the copper interconnect. Noise in the ceramic layers is due to the presence of interfaces and the surface roughness of the soldered connection; this is only an artifact and is not used for any calculations.

affecting the measured value of temperature or voltage. By simultaneously measuring the open-circuit voltage, ΔV_{OC} and the temperature drop across the TE legs, ΔT, the effective Seebeck coefficient of the module is defined as

$$\alpha = \lim_{\Delta T \to 0} \frac{\Delta V_{OC}}{\Delta T} \approx \frac{\Delta V_{OC}}{\Delta T}, \quad (4)$$

where α is the Seebeck coefficient, ΔV_{OC} is the measured open-circuit voltage, and ΔT is the temperature difference.

Infrared imaging also allows for high spatial resolution detection of material and interfacial defects by observing anomalies in the thermal signature of a device in operation. TE modules tend to fail at the interconnect–leg interface due to thermal cycling and the consequential thermomechanical stresses caused by large temperature gradients.[14] Cracks and physical damage may be difficult to detect optically but are well defined in their thermal signature when heating occurs in a damaged region. A crack behaves as an interface with high thermal resistance, and this causes the isotherms to shift and rotate. Cracks appear on the IR image in the form of hotspots due to localized high electrical resistance and subsequent Joule heating at the defect.[18] Nonuniformities in the one-dimensional temperature profile may also indicate changes at the atomic level, including diffusion and material degradation. By imaging in the infrared spectrum with a spatial resolution up to the diffraction limit it is possible to rapidly observe and assess material changes and device failure modes that are difficult to detect optically.

Harman Method for Determining Electrical Conductivity and Figure of Merit

The Harman method is used to determine the electrical resistivity and TE figure of merit for the module.[15,19] A DC current source (Keithley 6221) connected to the TE module applies 10 mA DC current, creating a small temperature difference and a voltage drop across the TE module, which is detected by a voltmeter (HP 3458A). This current was chosen to be large enough to give a stable signal but small enough to minimize the total temperature rise. The resulting voltage has both an electrical component due to the current flowing through a finite electrical resistance and a thermoelectrical component due to the nonzero temperature difference across the module. The 10 mA DC current is applied for 70 s, which is sufficient time for the system to reach thermal steady state as determined by the stability of the voltage. The current source is then turned off. Since the thermal time constant is substantially larger than the electrical time constant, this eliminates the electrical contribution of the voltage, leaving only the thermoelectric component due to the heat capacity of the module. The TE module is then allowed to cool for 60 more seconds, during which time the TE module reaches thermal equilibrium with the ambient conditions and the thermoelectric voltage decays to zero. A representative voltage trace is shown in Fig. 4.

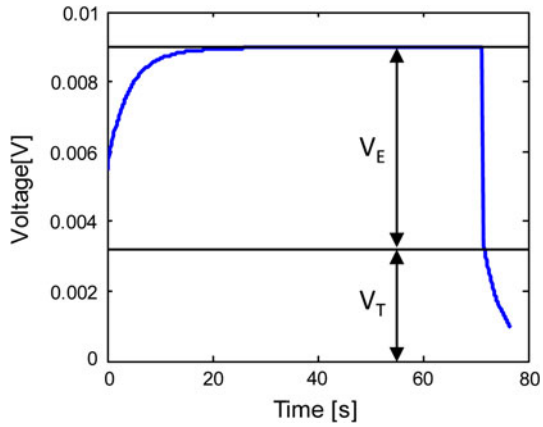

Fig. 4. Example Harman method voltage trace for applied current of 10 mA for 70 s. V_{total} is the combined electrical and thermoelectrical voltage. V_E and V_T are the electrical and thermoelectrical voltages, respectively. The transient regions ($t <$ 30 s, $t >$ 70 s) correspond to the thermal response time while the thermoelectrical component of voltage reaches steady state. The electrical component response time is extremely short and is effectively undetectable compared with the thermal response time.

This is repeated at least ten times during each measurement interval, and the results are averaged to ensure an accurate analysis. The total voltage is measured just before the current source is stopped, and the thermoelectric voltage is measured immediately after the removal of the current. The electrical contribution to voltage is the difference between these two values, corresponding to the sudden voltage drop in Fig. 4. Using Ohm's law with a fixed DC current and a measured electrical voltage, the electrical resistance of the module is calculated.

Harman et al.[15] present the following definitions based on first principles for the individual thermoelectric properties:

$$\rho = \frac{V_E A_{TE}}{IL}, \quad (5)$$

where ρ is the electrical resistivity, V_E is the electrical component of voltage, I is the electrical current, and L is the length of the element;

$$\alpha = \frac{V_T}{\Delta T}, \quad (6)$$

where α is the Seebeck coefficient, V_T is the thermoelectric component of voltage, and ΔT is the temperature difference; and

$$k = \frac{\alpha I T L}{\Delta T A_{TE}}, \quad (7)$$

where k is the thermal conductivity, T is the mean temperature, and A_{TE} is the cross-sectional area of the element.

These terms are substituted into Eq. 1, where $\sigma = \rho^{-1}$, to calculate ZT from measured properties.

The TE figure of merit ZT is calculated from the same voltage trace[15]

$$ZT = \frac{V_T}{V_E}. \quad (8)$$

These expressions are valid for a small temperature difference across the module, which is proportional to the supplied current. For these measurements with an applied current of 10 mA, the temperature difference across the TE module is estimated to be $\ll 1°C$ at steady state. This maintains the module at approximately the ambient temperature during the measurement, which reduces the impact of temperature-dependent properties. This also ensures that the analysis is accurate using the linear approximation presented in the original Harman solution.

RESULTS AND DISCUSSION

Thermoelectric Module Failure Mode Analysis

For a constant applied DC voltage, the resulting temperature range during thermal cycling decreases over time, while the thermal time constant of the TE module dramatically increases. Initially, with $V_{pp} = \pm 2.3\ V_{DC}$, the temperature range of the convective side of the TE module is observed to be +146°C to −20°C. At ~45,000 cycles, this same voltage signal produces a temperature range of only +40°C to +20°C. This indicates that the TE module has effectively failed. This sudden degradation is hypothesized to be largely due to interface degradation and the formation of defects near the interfaces, which increase the electrical resistivity by several orders of magnitude. This agrees with finite-element simulations, which indicate that the peak thermomechanical stresses are located at the surface of the interfaces.[14]

Baseline IR temperature maps were recorded before cycling to verify the uniformity associated with unstressed TE elements (Fig. 5). After 45,000 cycles, there are multiple TE legs that exhibit thermal signatures characteristic of mechanical damage. Often the nonuniform temperature distribution results from a partial crack at the soldered interface, as verified using scanning electron microscopy (SEM). Many of the legs are found to have nonparallel isotherms as shown in Fig. 6, indicating that heat is no longer flowing uniformly through the TE material. This is likely due to a combination of material degradation near the interface region and the interfacial defects. The formation of defects at the leg–interconnect junction is not always optically visible, but the effects of mechanical degradation can be readily observed using the IR microscope to detect changes in the thermal signature of the operating device. The degraded region appears as a bright line on the IR temperature map, potentially due to high electrical contact resistance, and skews the isotherms along the TE leg. The presence of cracks, cavities, or other defects at the boundaries may also distort the local radiant emission and is easily identifiable in the thermal signature of the surface. While IR imaging is a tool which provides rapid damage assessment of thermoelectric devices, it cannot independently resolve the multiple parallel degradation mechanisms that are present.

Mechanical damage is also observed directly by SEM of the surface of the TE leg and interface (Fig. 7). Prior to thermal cycling, SEM images indicate a high degree of consistency and uniformity within each of the TE legs and interfaces. After device failure, additional SEM images were taken which reveal a large population of defects, cracks, and other mechanical damage (to varying degrees) in the vicinity of the interfaces for nearly all of the individual TE elements. While these observations suggest one possible failure mode, multiple degradation mechanisms contribute in parallel to the overall performance reduction. For example, diffusion of atomic species at the interfaces also contributes to changes in the thermoelectric properties of the device.[17] The relative contribution of the different failure modes is not independently quantified in the present work.

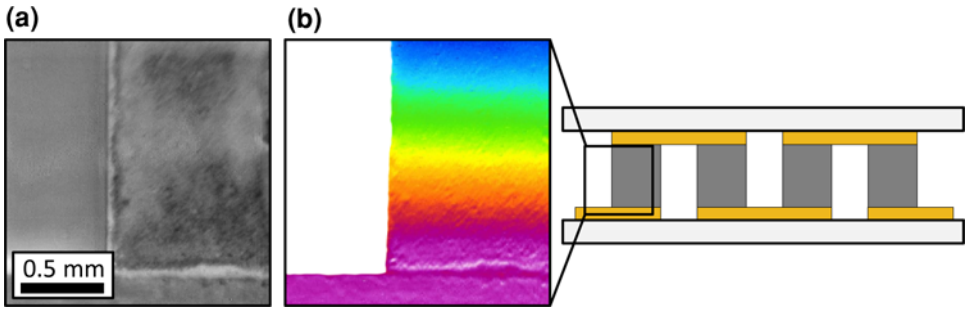

Fig. 5. (a) Optical and (b) infrared image of the interface between a TE leg and a copper interconnect. As heat conducts through the interconnect and the TE leg, we can identify damage by examining nonuniformities in the temperature map. This image was taken prior to thermal cycling. As a result, the temperature map is smooth and linear with uniform isotherms, indicating an undamaged TE leg and a mechanically stable solder interface.

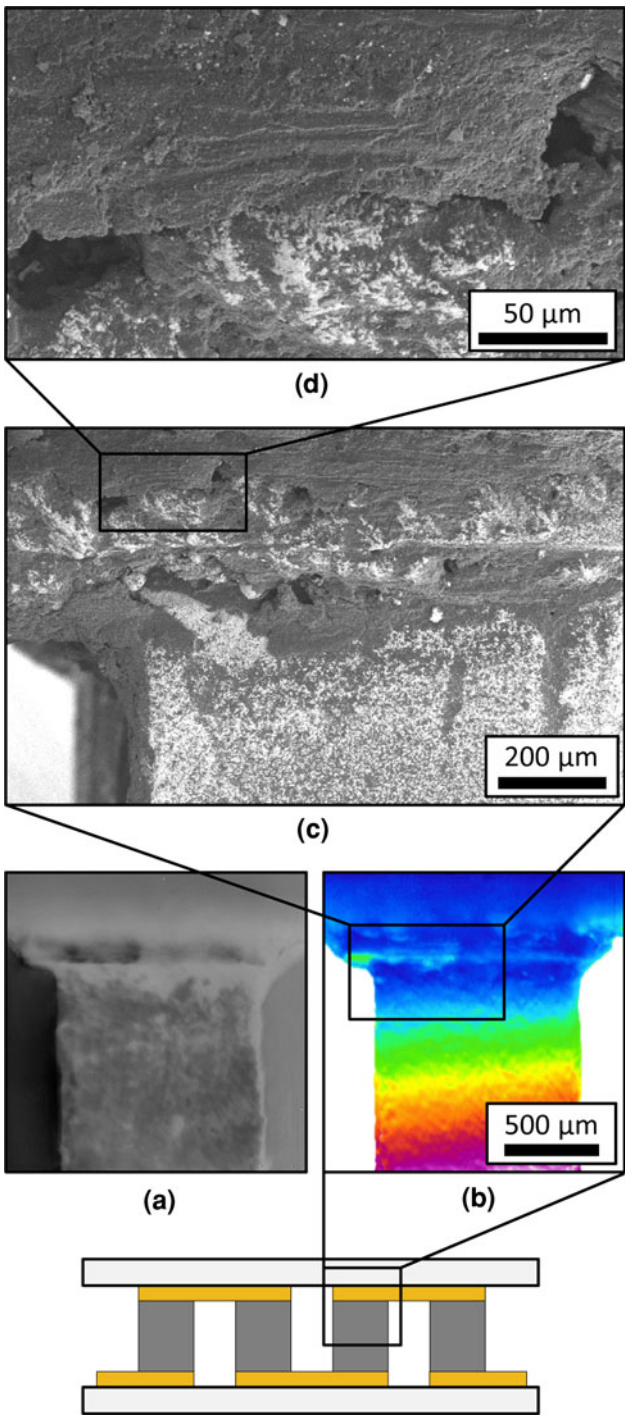

Fig. 6. (a) Optical and (b) infrared image of a damaged solder interface between the interconnect and TE leg. Here a crack is visible on the left half of the interface in the infrared image. The mechanical damage is not apparent in the optical image alone. However, the temperature nonuniformity and nonparallel isotherms in the IR imaging allow rapid assessment of the extent of thermomechanical damage at the brittle solder bonds. (c) SEM micrograph showing the presence of a defect in the solder interface. (d) SEM micrograph showing higher resolution of an individual defect. This confirms the presence of defects at the interface which contribute to the irregular thermal signature shown in the infrared image.

Thermoelectric Figure of Merit

The TE figure of merit was calculated directly using the Harman method at predetermined measurement intervals during thermal cycling, and the results are shown in Fig. 8. The baseline measurement yielded a figure of merit value of $ZT = 0.624$. Module performance degrades gradually during the first 10,000 cycles. Between 10,000 and 45,000 cycles, performance drops substantially, eventually leading to complete device failure. While the thermal voltage during the characterization of ZT drops slightly after failure, the electrical voltage increases by more than an order of magnitude. Combined with the failure mode analysis discussed previously, this is indicative of a large electrical contact resistance being introduced into the system. The reduction in ZT is the first major indicator of reduced TE module performance under cycling. The reduction is most dramatic after 10,000 cycles as the device begins to break down mechanically. There is a steady decline in ZT prior to 40,000 cycles, and then there is an abrupt reduction once the device fails. At the point of critical failure (45,000 cycles), ZT was reduced to $ZT = 0.0197$, or 3.16% of the initial value.

The original technique presented by Harman et al. is derived from an analysis of a single thermoelectric material. There is additional uncertainty in the present analysis of a complete thermoelectric module due to the complexities introduced through the metallic bonding layers, the copper interconnects, the ceramic insulators, and the pairs of dissimilar TE elements. While this does not strongly affect the measurement of the electrical voltage, there are some inaccuracies associated with the direct extraction of the thermoelectric figure of merit as derived by the original Harman analysis. This method does, however, allow for the rapid assessment of an *effective* figure of merit which is self-consistent throughout thermal cycling and can demonstrate trends in the evolution of ZT with cycling. In addition, the effects of convection and radiation, as well as conduction to the ceramic insulator, contribute to deviations from the ideal analysis of intrinsic properties.

Thermal Conductivity, Electrical Conductivity, and Seebeck Coefficient

The individual components of ZT were subsequently investigated to illuminate the degree to which each component contributes to this performance reduction. At each measurement interval, the electrical conductivity, thermal conductivity, and Seebeck coefficient were measured independently. A baseline value was measured for each property prior to cycling in order to establish the values for an unstressed TE module. Subsequent measurements after cycling are considered relative to this baseline.

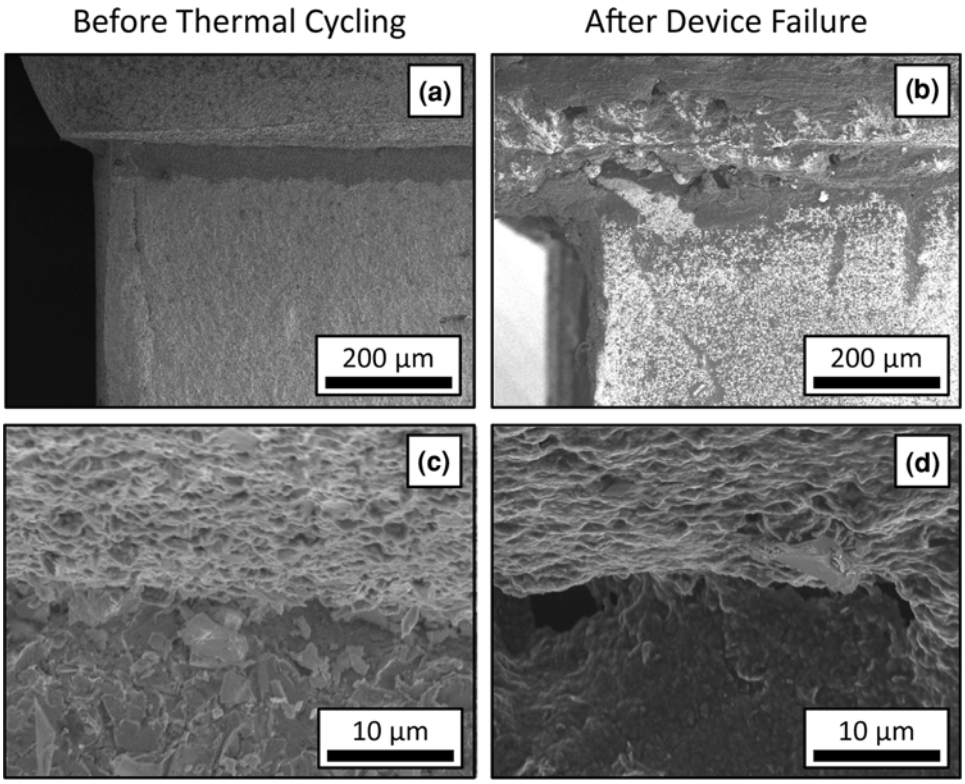

Fig. 7. The interface between an individual TE leg and a copper interconnect is shown in an SEM image (a) before thermal cycling and (b) after device failure. Thermal cycling is found to induce a high density of pores and other mechanical defects in the vicinity of the interface. By examining the interfacial junction more closely (c) before and (d) after thermal cycling, these defects were found to comprise a combination of voids, pores, and cracks.

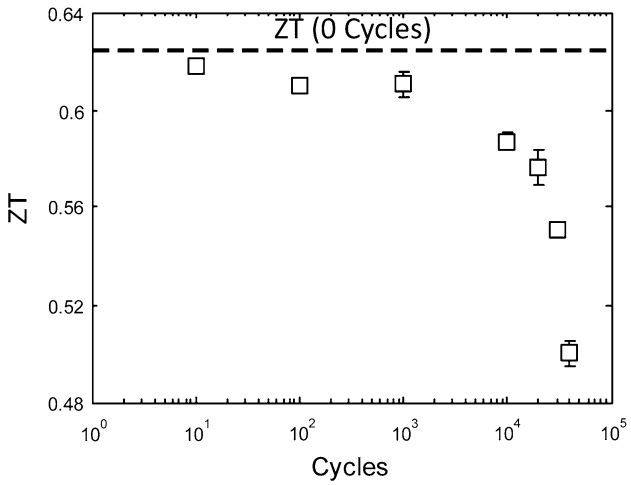

Fig. 8. Effect of thermal cycling on the TE figure of merit as measured using the Harman method. These data demonstrate the continuous reduction in TE performance up to critical failure (not shown). After 10,000 cycles, ZT rapidly decreases with cycling. Each data point represents the mean value from a minimum of ten independent measurements with error bars indicating a spread of one standard deviation. Statistical variations in the measurement arise primarily from uncertainty in V_E and V_T, which is limited by the temporal resolution of the voltmeter.

The electrical conductivity experiences the largest degradation of the individual thermoelectric properties with cycling. The electrical resistance increases monotonically with cycles as shown in Fig. 9, which is likely caused by the increased contact resistance at the solder joints due to the formation of microcracks. Thermoelectric devices operate electrically in series, and as thermal cycling induces microscopic damage along the electrical current path, each new contact resistance is added into the net resistance of the module. The resistance increases from $R = 0.551\ \Omega$ prior to thermal cycling up to $R = 0.675\ \Omega$ after 40,000 cycles, a 22% increase. At 45,000 cycles, when the device fails, the net effect of contact resistance increases the electrical resistance by a factor of $\sim$30 to $R = 16.2\ \Omega$.

The thermal conductivity of two adjacent TE legs was measured at each cycling interval to ensure that both n- and p-type legs were considered. The measured thermal conductivity was $k = 0.837 \pm 0.138\ \mathrm{W\ m^{-1}\ K^{-1}}$ for the pair of legs at an average temperature of 50°C. The thermal conductivity of the module (as opposed to the electrical conductivity) is less affected by the formation of interfacial microcracks since the TE elements are thermally in parallel. Additionally, the IR measurement technique allows separation of the thermal conductivity of the module elements from the thermal resistance at the interfaces. Thus, the slight increase in thermal conductivity with thermal cycling is likely due to material changes and diffusion near the soldered

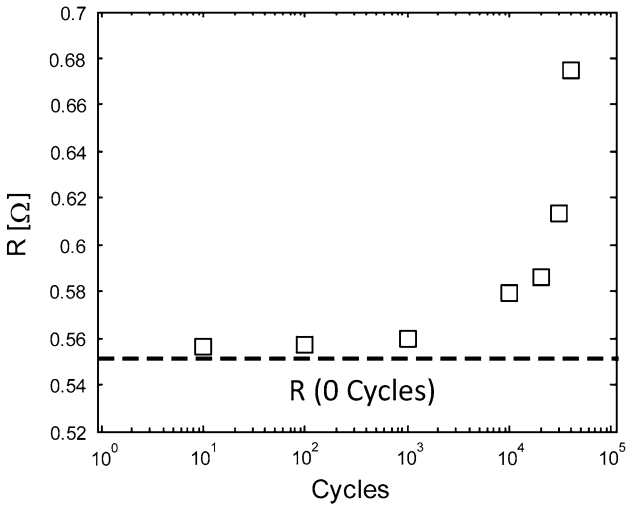

Fig. 9. Effect of thermal cycling on the electrical resistance of the TE module. Electrical resistance increases monotonically with the number of thermal cycles. This is attributed primarily to the formation of microcracks which increase the contact resistance. The large increase in electrical resistance is the primary cause for the reduction in ZT with cycling. Each data point represents the mean value from a minimum of ten independent measurements with error bars indicating a spread of one standard deviation, being approximately the size of the marker. Statistical variations in the measurement arise primarily from uncertainty in V_E and V_T, which is limited by the temporal resolution of the voltmeter.

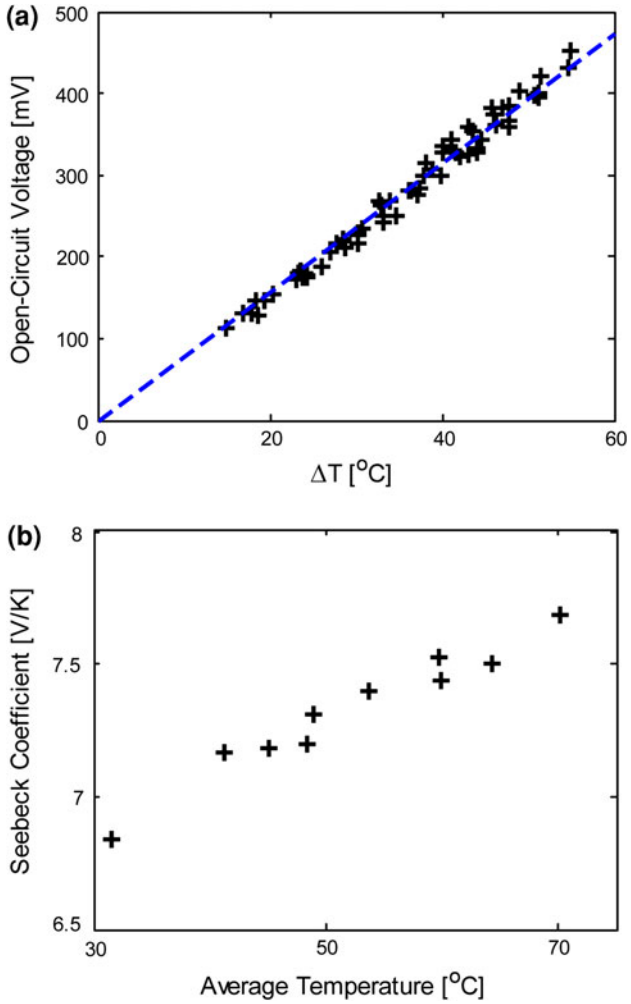

Fig. 10. (a) Open-circuit TE module voltage as a function of temperature difference across the TE module. The slope of this plot yields the Seebeck coefficient. During thermal cycling, these data continue to fall along the same line, indicating that the Seebeck coefficient is stable. There is a slight nonlinear deviation for larger temperature gradients, which is due to the temperature dependence of the Seebeck coefficient. These data points include all measurements taken at each cycling interval prior to device failure from 0 to 40,000 cycles. (b) Seebeck coefficient as a function of mean TE module temperature. The mean temperature of the TE module is taken as the mean temperature of the inner side of the hot- and cold-side ceramic plates. Over the range of measured temperatures, the Seebeck coefficient increases monotonically with temperature from 30°C to 70°C. Data shown are the baseline measurement at 0 cycles, but this trend is consistent at each cycling interval.

junctions and interconnects, which requires additional sample characterization not presented in this work.

The Seebeck coefficient is measured after the TE module reaches a stable temperature gradient and open-circuit voltage. The open-circuit voltage and temperature difference are compared to extract the Seebeck coefficient using Eq. 4 (Fig. 10a). The Seebeck coefficient remains relatively stable to within 5% of the baseline value throughout the duration of the thermal cycling and has a negligible effect on the reduction of ZT during cycling. For each measured Seebeck coefficient value, the mean temperature is measured between the hot side and cold side of the interior of the module. As shown in Fig. 10b, the Seebeck coefficient increases by 12% with increasing temperature from 30°C to 70°C.

The figure of merit ZT depends linearly on the electrical conductivity, as shown in Eq. 1. Figure 11 shows the evolution of each thermoelectric property normalized to the baseline value with thermal cycling. At 45,000 cycles, the most significant thermoelectric property change is the decrease in electrical conductivity (by a factor of 29.4). Therefore, due to the reduction of the electrical conductivity, ZT is expected to decrease to 3.40% of the baseline value. In comparison, using the Harman method at 45,000 cycles to directly measure the figure of merit yields ZT = 0.0197, or 3.16% of the baseline value. The additional reduction in ZT beyond that resulting from the electrical conductivity is due to the combined effect of small changes in the thermal conductivity and the Seebeck coefficient with thermal cycling.

In the present work, observable defects are found in the vicinity of the interfaces, which contribute to the performance degradation of the module. However, it is also possible that material changes and diffusion can contribute to these performance changes in both the thermal and electrical conductivity. Quantifying the relative contribution of mechanical and material degradation mechanisms requires additional experimentation.

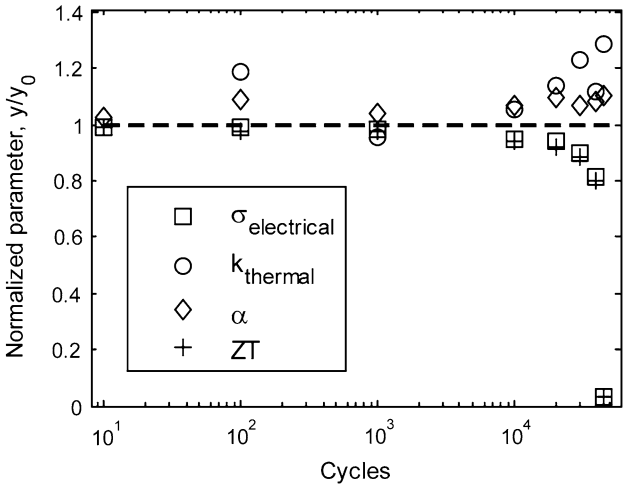

Fig. 11. Evolution of thermoelectric properties and the figure of merit during thermal cycling. This shows normalized individual thermoelectric properties as a function of the number of thermal cycles, where all values are normalized relative to the baseline value measured at 0 cycles. These data represent measurement intervals in the thermal cycling from 0 cycles through the point of device failure at 45,000 cycles. Thermal conductivity increases by ~20% over the baseline value. The electrical conductivity demonstrates the largest deviation with thermal cycling and decreases by a factor of ~30 after 45,000 cycles. The Seebeck coefficient remains stable during the lifetime of the device. Consequently, *ZT* drops to 3.16% of the original value.

CONCLUSIONS

The thermoelectric performance of a sample module continuously degrades with thermal cycling, ultimately leading to complete device failure at 45,000 cycles. The point of failure is indicated by (1) a sharp reduction in the figure of merit *ZT* and the operating temperature range under sustained voltage, (2) a factor of ~30 increase in the electrical resistance, and (3) the formation of microscopic cracks at the TE leg–interconnect interface. Defect formation at the interfaces is observed and likely contributes to a rapid increase in electrical resistance due to interfacial contact. The increased electrical resistance reduces *ZT* to 3.40% of the initial value prior to cycling. An additional reduction to 3.16% of the initial value is attributed to small changes in the thermal conductivity and the Seebeck coefficient of the module. Ongoing work to address these design issues focuses on the use of nanostructured thermal interface materials to alleviate interfacial thermomechanical stresses while providing good thermal and electrical conduction across the interface.

ACKNOWLEDGEMENTS

The authors gratefully acknowledge financial support from the National Science Foundation and Department of Energy Partnership on Thermoelectric Devices for Vehicle Applications (Grant No. 1048796), the National Defense Science and Engineering Graduate Fellowship Program, the National Science Foundation Graduate Research Fellowship Program, the Stanford Graduate Fellowship Program, and the Korea Institute of Energy Technology Evaluation and Planning Fellowship Program. The SEM micrographs are courtesy of Yuan Gao.

REFERENCES

1. K. Zorbas, E. Hatzikraniotis, and K. Paraskevopoulos, *5th European Conf. of Thermoelectrics*, Odessa, Ukraine (2007).
2. J. Yang and T. Caillat, *MRS Bull.* 31, 224 (2006).
3. K. Zorbas, E. Hatzikraniotis, K. M. Paraskevopoulos, and Th. Kyratsi, *AIP Conf. Proceedings*, vol. 1203, pp. 1137–1142 (2010).
4. E. Hatzikraniotis, *International Congress on Advances in Applied Physics and Materials Science*, Antalya, Turkey, pp. 287–289 (2012).
5. S. LeBlanc, Y. Gao, and K. E. Goodson, *Proc. of IMECE*, Boston, MA, pp. 1–7 (2008).
6. E.W. Miller, T.J. Hendricks, and R.B. Peterson, *J. Electron. Mater.* 38, 1206 (2009).
7. I. Chowdhury, R. Prasher, K. Lofgreen, G. Chrysler, S. Narasimhan, R. Mahajan, D. Koester, R. Alley, and R. Venkatasubramanian, *Nat. Nanotechnol.* 4, 235 (2009).
8. L.E. Bell, *Science* 321, 1457 (2008).
9. Y. Yang, X.-J. Wei, and J. Liu, *J. Phys. D Appl. Phys.* 40, 5790 (2007).
10. G.J. Snyder and E.S. Toberer, *Nat. Mater.* 7, 105 (2008).
11. D.L. Medlin and G.J. Snyder, *Curr. Opin. Colloid Interface Sci.* 14, 226 (2009).
12. E. Hatzikraniotis, K.T. Zorbas, I. Samaras, T. Kyratsi, and K.M. Paraskevopoulos, *J. Electron. Mater.* 39, 2112 (2009).
13. Y. Gao, A.M. Marconnet, M.A. Panzer, S. LeBlanc, S. Dogbe, Y. Ezzahri, A. Shakouri, and K.E. Goodson, *J. Electron. Mater.* 39, 1456 (2010).
14. Y. Hori, D. Kusano, T. Ito, and K. Izumi, *Eighteenth International Conference on Thermoelectrics* (2000).
15. T. C. Harman, J. H. Carn, and M. J. Logan, *J. Appl. Phys.* 30 (1959).
16. D.M. Rowe and G. Min, *J. Power Sources* 73, 193 (1998).
17. Y.C. Lan, D.Z. Wang, G. Chen, and Z.F. Ren, *Appl. Phys. Lett.* 92, 101910 (2008).
18. R.G. de Villoria, N. Yamamoto, A. Miravete, and B.L. Wardle, *Nanotechnology* 22, 185502 (2011).
19. W. Park, M.T. Barako, A.M. Marconnet, M. Asheghi, and K.E. Goodson, *Proc. of ITHERM*, San Diego, CA (2012).